Unraveling the superior role of dicarboxylic acids as surface chelators in Eu^{3+}-doped yttrium fluorides: a systematic modulation of the crystal phases and morphologies for highly tuned optical performance

Pablo Serna-Gallén (pserna@uji.es), Héctor Beltrán-Mir* (mir@uji.es), Eloísa Cordoncillo* (cordonci@uji.es)

Departamento de Química Inorgánica y Orgánica, Universitat Jaume I, Av. Sos Baynat s/n 12071, Castelló de la Plana, Spain

*Corresponding Authors

Abstract

Eu^{3+}-doped YF_3 and KY_3F_{10} phosphors have been prepared hydrothermally in a wide range of pH values without the use of surface chelators and adding oxalic or tartaric acid. We have proved, for the first time, the usefulness of dicarboxylic acids to modulate the evolution of the surface and crystal phases in the KF-YF_3 system. The morphologies and crystal structures of the materials displayed a critical dependence on the pH and the chelator employed, and a plausible mechanism to explain the differences among the distinct series of samples is proposed. As a result, the fluorides exhibited outstanding and tunable photoluminescence, with extremely high quantum efficiencies and very long lifetimes. The asymmetry ratio and Judd-Ofelt parameters calculations allowed us to establish a relationship between the optical performance of the compounds and their physicochemical properties. We feel that this study can arouse widespread interest within the materials engineering community, since similar procedures could be implemented to the extended family of complex yttrium/lanthanide fluorides for advanced applications in important fields such as bioanalytics, biomedics, or photonics. Indeed, the materials in the present work, with orangish-yellow colored emissions, could be very interesting for application in white

light emitting diodes through their combination with blue chips.

Keywords: fluoride, europium, optical spectroscopy, luminescence, surface chelator, structure

Graphical Abstract:

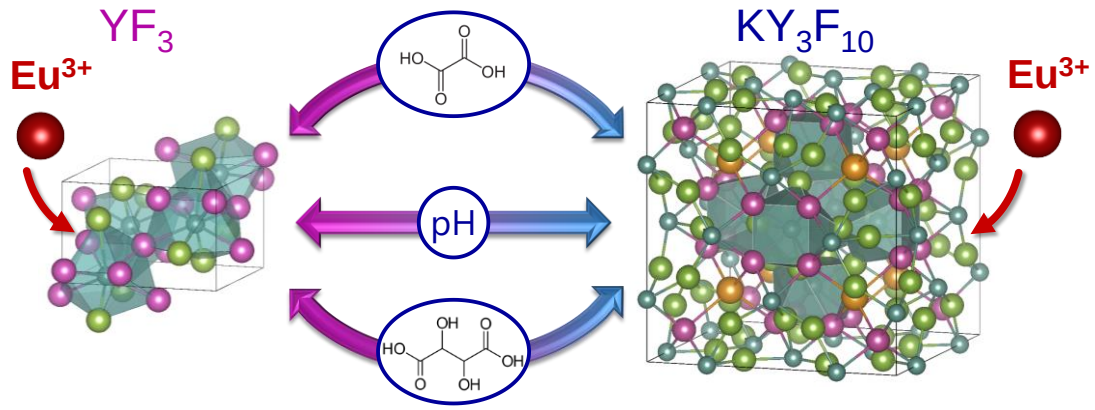

1. Introduction

Over the last few years, there has been an increasing interest in materials doped with luminescent lanthanide ions (Ln^{3+}) because of their wide-ranging potential applications in various fields, such as emitting diodes, solar cells, lasers, or catalysts [1–3]. Among many inorganic materials, fluorides are the most appealing candidates for optical applications because of their low phonon energy associated with the crystal lattice [4]. Consequently, fluoride-based materials present high quantum efficiencies with long lifetimes of Ln^{3+} ions that vary from a few microseconds to several milliseconds [5]. Due to their electronic features arising from the 4*f* electrons and the possibility of energy transfers, many studies have used fluoride phosphors as up/down-converters for efficient spectral conversion [6–8]. Additionally, Ln^{3+}-doped fluorides are of great interest for bioanalytical and biomedical applications. Besides the above-mentioned characteristics, the excellent photostability, low cytotoxicity, and narrow emission lines

of these materials make them potential biomarkers for *in vivo* imaging [9–11].

Fluoride hosts with trivalent lattice cations such as Y^{3+} are considered of paramount importance for photoluminescence because Y^{3+} ions can easily be replaced by isovalent lanthanide ions [12]. Among them, both YF_3 and the crystalline compounds of the related KF-YF_3 system (KYF_4, KY_3F_{10}, K_2YF_5, etc.) doped with Ln^{3+} ions have shown outstanding optical response. In particular, YF_3 is considered one of the most significant host lattices for achieving efficient up/down-conversion emissions, and KY_3F_{10} has recently been drawing special interest [13–15]. Commonly, $NaYF_4$ has been coined as the best fluoride matrix. Nevertheless, some studies have demonstrated the usefulness of YF_3 over $NaYF_4$ to realize high up-conversion efficiency [16,17]. On the other hand, the thermodynamic stability of KY_3F_{10} is higher than that of $NaYF_4$, which often suffers phase transitions with temperature that can affect the repeatability of fluorescence-intensity-ratio-based optical thermometry measurements [18]. All these remarks emphasize the relevance of YF_3 and KY_3F_{10}, although they are both still subject to advanced research over a wide range of applications.

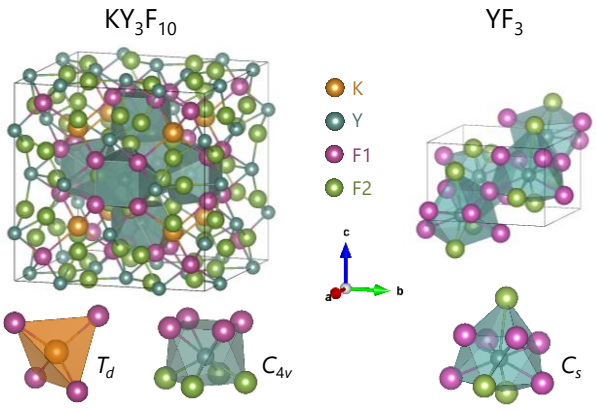

Figure 1. Structure of cubic KY_3F_{10} and orthorhombic YF_3 highlighting the coordination polyhedra of Y^{3+} and K^+ ions along with their local symmetry. The labels F1 and F2 refer to fluoride anions situated at different Wyckoff positions.

Under ambient conditions, KY_3F_{10} crystallizes in a cubic structure belonging to the $Fm\bar{3}m$ (O_h^5) space group, with 8 formula units per unit cell (Z = 8) [19], while YF_3 crystallizes in an orthorhombic structure with the $Pnma$ (D_{2h}^{16}) space group, and Z = 4 [20]. The unit cell structure of KY_3F_{10} and YF_3 crystals, the coordination polyhedra of Y^{3+} and K^+, and their local symmetry plotted with VESTA software [21] are depicted in Figure 1.

The luminescence properties of the materials depend to a great extent on their chemical reaction engineering, which opens up new strategies for the design and surface control of materials. To date, different methods have been used to synthesize nano/micron-sized fluorides [22–24]. Particularly, the hydrothermal method has been shown to be the most effective technique to control the morphologies, sizes, crystal phases, and color emissions of inorganic materials [25,26].

Although Ln^{3+}-doped fluorides with several shapes and sizes have been prepared in the literature with different capping agents that allow their surface modification, the vast majority have been synthesized by using hydrophobic organic molecules such as oleic acid, which results in hydrophobic surfaces [27,28]. As a consequence, the hydrophobicity prevents these materials from being used directly for bioapplications since neither good stability in water nor effective bioconjugation can be achieved without further surface modifications.

In light of this, different hydrophilic organic molecules can be used to replace the oleic acid ligand in the synthesis of these materials. Polydentate carboxylic ligands are regarded as excellent candidates because of the direct carboxylic-to-metal coordination [29], citric acid and ethylenediaminetetraacetic acid (EDTA) being the most common [30–33]. Nevertheless, the role of dicarboxylic acids (such as oxalic, tartaric, or

malonic acid, to name but a few) has been almost entirely neglected in the literature and studies that report their use in the synthesis of the extended family of yttrium/lanthanide fluorides are scarce. Besides, the few that do use dicarboxylic acids have focused primarily only on $NaLnF_4$ compounds (Ln = Y, La to Lu) disregarding other types of fluorides [34–37]. Indeed, to the best of our knowledge, no attempts have been made to prove whether the use of dicarboxylic ligands in the KF-YF_3 system can be successful or not. Therefore, from a chemical engineering point of view, the need to explore the usefulness of these capping agents in such materials is a matter of importance because they could also be applied to a vast gamut of compounds.

Based on the remarks made in the foregoing paragraphs, in this paper we further investigate Eu^{3+}-doped YF_3 and KY_3F_{10} materials prepared by a hydrothermal method using KBF_4 as the fluoride source. We have chosen Eu^{3+} as a dopant ion because of its unique luminescent properties and its adequacy as a site-sensitive structural probe [38], which is a keystone to describe the optical response of the materials and relate it to their chemical structure. Moreover, the similarity between the ionic radius of Y^{3+} (1.019 Å for a coordination number, CN, = 8; 1.075 Å for a CN = 9) and Eu^{3+} (1.066 Å for a CN = 8; 1.120 Å for a CN = 9) [39] ensures good incorporation of the Eu^{3+} ions in the YF_3/KY_3F_{10} host lattices.

Here, we report for the first time the effective use of dicarboxylic acids (oxalic and tartaric acid) as chelating agents to control the surface and thus the evolution of the crystal phase between YF_3 and KY_3F_{10}. We show that the pH is also crucial to obtain the crystal phase with different morphologies and we propose a plausible mechanism to explain the results obtained. All these parameters make it possible to achieve materials with tunable optical properties.

2. Experimental section

2.1. Materials

The reagents used were yttrium(III) nitrate hexahydrate [$Y(NO_3)_3 \cdot 6H_2O$ 99.9%, Alfa Aesar], europium(III) nitrate hexahydrate [$Eu(NO_3)_3 \cdot 6H_2O$ 99.9%, Strem Chemicals], potassium hydroxide [KOH 85%, Labkem], potassium tetrafluoroborate [KBF_4 96%, Sigma-Aldrich], nitric acid [HNO_3 65%, Labkem], oxalic acid dihydrate [$C_2H_2O_4 \cdot 2H_2O$ 99.5%, Panreac], and DL-tartaric acid [$C_4H_6O_6$ 99%, Sigma-Aldrich].

2.2. Synthesis of Eu^{3+}-doped compounds

In a typical synthesis procedure, 1.5 mmol $Ln(NO_3)_3 \cdot 6H_2O$ were dissolved in 30 mL of water (Ln = Y, Eu; 1 mol% Eu^{3+}) with a resulting pH of 4. Then 3.0 mmol of KBF_4 were added to this solution and the pH was adjusted to the desired value (pH = 4, 6, 7, 8, and 10) using 0.1 or 2 M KOH aqueous solutions (for pH values higher than 7, a whitish precipitate appeared). The mixture was kept under vigorous stirring for 10 min and the final volume was adjusted to 50 mL with water. The whole system was transferred into a Teflon-lined vessel (with a total volume of 125 mL) and treated hydrothermally for 24 h in a thermally heated autoclave at 180ºC. After cooling to room temperature, the product was collected by centrifugation, washed several times with water, and dried under an infrared lamp. The as-obtained powders were ground in an agate mortar to obtain a fine powder and break up any large aggregates.

To investigate the effect of the incorporation of dicarboxylic acids acting as chelating agents (oxalic and tartaric acid, OA and TA, respectively), the synthesis was performed in a similar manner. After obtaining the Ln^{3+} solution and before adding KBF_4, 3.0 mmol of oxalic/tartaric acid were dissolved in 10 mL of water. The pH of this

solution was adjusted to 6.5 using 2 M KOH aqueous solution, and it was stirred for 10 min. It was then added to the previous Ln^{3+} solution dropwise with stirring, and the mixture was stirred for another 10 min. After that, 3.0 mmol of KBF_4 were added and it was performed in the same way as in the typical reaction. Table 1 summarizes the abbreviations of the different samples according to the pH value and the chelator used in each synthesis. Some considerations about the experimental procedure when using chelating agents can be found in the Supplementary Information (Section 1).

Table 1. Nomenclature of the different Eu^{3+}-doped compounds prepared by a hydrothermal process with different pH values and chelating agents.

pH	No Chelator	Oxalic Acid	Tartaric Acid
4	H4	H4-OA	H4-TA
6	H6	H6-OA	H6-TA
7	H7	H7-OA	H7-TA
8	H8	H8-OA	H8-TA
10	H10	H10-OA	H10-TA

2.3. Characterization

All the characterization was performed at room temperature. Powder X-ray diffraction (XRD) was performed using a Bruker-AX D8-Advance X-ray diffractometer with Cu$K_{\alpha 1}$ radiation from $2\theta = 20$ to 90º and at a scan speed of 2.25º/min. The unit cell parameters were refined using the $WinX^{POW}$ software package, version 1.06. The microstructure of samples was observed using a JEOL 7001F scanning electron microscope (SEM) operating with an acceleration voltage of 15 kV, a measuring time of 20 s, and a working distance of 10 mm. For microstructural characterization, the powders were deposited on carbon double-sided stickers (previously adhered to the surface of aluminum stubs) and were sputtered with platinum.

The optical properties were studied with an Eclipse Fluorescence Spectrophotometer (Varian). All the photoluminescence measurements were performed in a standard way by placing the powders in a solid sample holder provided by Agilent Technologies. Excitation spectra were recorded in the 250–500 nm range with an emission wavelength of 593 nm. Emission spectra were performed upon excitation at 395 nm in the 500–750 nm range and normalized to the magnetic dipole $^5D_0 \rightarrow {}^7F_1$ transition. The asymmetry ratio R, the branching ratios (β_i), and the Judd-Ofelt parameters (Ω_2 and Ω_4) were calculated from the spectra. The integrated emission intensities of the samples were obtained from the integrated area under the corresponding emission spectra. Besides, the CIE coordinates of the Eu^{3+}-doped materials were calculated from the emission spectra using the GoCIE software package. Time-resolved luminescence measurements were also performed at different emission wavelengths, with the excitation wavelength monitored at 395 nm. Lifetime values were extracted from decay profiles.

3. Results and discussion

3.1. Structural characterization

The XRD patterns of the Eu^{3+}-doped powders obtained at different pH values following a hydrothermal synthesis are depicted in Figure 2. Figure 2(a) corresponds to the samples synthesized without the incorporation of chelating agents. In this series of samples, interesting changes appear depending on the pH of the medium. The XRD patterns of samples H4, H6, and H7 (with a pH of 4, 6, and 7, respectively) exhibit all the peaks corresponding to the orthorhombic phase of YF_3 (JCPDS-ICDD card 321431). However, H4 and H6 present broad, low-intensity peaks, whereas H7 presents narrow,

high-intensity peaks. These changes in the shape and intensity of the XRD peaks are attributed to differences in the crystallinity and size of the materials (micro/nano-sized) as will be discussed later. Another interesting detail is that the relative intensities of the peaks with Miller indices (101), (020), (111), and (301) in the XRD patterns of YF_3 samples vary according to the structure of the particles, thereby indicating that the morphologies have different crystalline planes as their dominant surfaces [40]. On the other hand, remarkable results are found in samples synthesized with a pH equal to or higher than 7 (H7, H8, H10). The crystal structure of these samples evolves towards the formation of cubic KY_3F_{10} (JCPDS-ICDD card 409643). Thus, the acidity of the medium in the hydrothermal treatment without the addition of chelators plays an important role in the crystal structure and final properties of the materials.

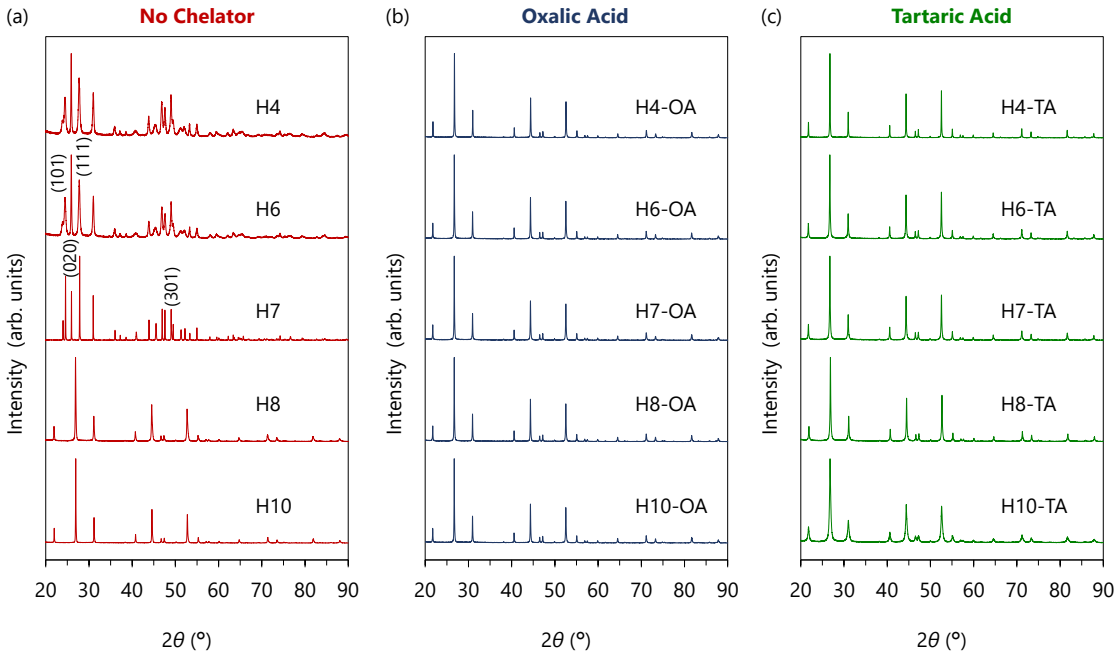

Figure 2. XRD patterns for the Eu^{3+}-doped compounds prepared at different pH values by a hydrothermal process (a) with no chelators, (b) using oxalic acid, and (c) adding tartaric acid as a chelating agent.

Figures 2(b) and 2(c) present the XRD patterns of powders synthesized following the hydrothermal route with the incorporation of oxalic and tartaric acid as chelating

agents, respectively. All the samples exhibited the cubic single-phase KY_3F_{10} in the total range of pH, in contrast to samples prepared without capping agents. The XRD profiles are quite similar with the proviso that the XRD peaks of samples prepared using tartaric acid become slightly broader with increased pH. As per the above comments, these results highlight the important chelating effect of oxalic and tartaric acid that allows us to control the crystal phase formation at different pH levels.

Additionally, the unit cell parameters of all the samples were refined and are indicated in Table 2. The values obtained were in good agreement with those reported for cubic KY_3F_{10} and orthorhombic YF_3, although no notable differences could be found between samples with the same crystal structure.

Table 2. Crystal phases and unit cell parameter *a* for the different Eu^{3+}-doped phosphors.

Sample	Crystal Phase	*a* (Å)[1]
H4	YF_3	6.3718(7)
H6	YF_3	6.3666(3)
H7	YF_3	6.3651(9)
H8	KY_3F_{10}	11.5348(2)
H10	KY_3F_{10}	11.5344(3)
H4-OA	KY_3F_{10}	11.5371(7)
H6-OA	KY_3F_{10}	11.5367(3)
H7-OA	KY_3F_{10}	11.5362(1)
H8-OA	KY_3F_{10}	11.5363(6)
H10-OA	KY_3F_{10}	11.5366(2)
H4-TA	KY_3F_{10}	11.5412(9)
H6-TA	KY_3F_{10}	11.5374(3)
H7-TA	KY_3F_{10}	11.5364(4)
H8-TA	KY_3F_{10}	11.5368(9)
H10-TA	KY_3F_{10}	11.5358(5)

[1] For the orthorhombic YF_3 compounds, the other unit cell parameters were: [H4: b = 6.8939(6), c = 4.4416(3)], [H6: b =6.8862(4), c = 4.4353(7)], and [H7: b = 6.8711(5), c = 4.4089(4)].

A plausible explanation of the reaction mechanism that leads the system towards the formation of YF_3 or KY_3F_{10} is discussed in the following. The reaction of Y^{3+} with oxalic and tartaric acid (H_2A) has been reported as producing two main products, namely YHA_2 and Y_2A_3, as shown in equations (1) and (2) [41,42].

$$Y^{3+} + 2H_2A \rightleftarrows YHA_2 + 3H^+ \quad (1)$$

$$2Y^{3+} + 3H_2A \rightleftarrows Y_2A_3 + 6H^+ \quad (2)$$

However, depending on the pH of the solution, other more complex species could also be formed, such as $[YA_2(OH)]^{2-}$ or YA(OH), among others [43]. Hence, in order to simplify the mechanistic explanations, the complex formed between Y^{3+} ions and the (de)protonated species of oxalic/tartaric acid is denoted by Y-complex. Without the addition of any chelating agents, the reactions leading to the formation of YF_3 or KY_3F_{10} would follow the steps (3)–(6).

$$BF_4^- + 3H_2O \rightleftarrows 3HF + F^- + H_3BO_3 \quad (3)$$

$$HF \rightleftarrows H^+ + F^- \quad (4)$$

$$Y^{3+} + 3F^- \rightarrow YF_3 \quad (5)$$

$$K^+ + 3Y^{3+} + 10F^- \rightarrow KY_3F_{10} \quad (6)$$

As the XRD results reveal, the pH of the initial solution is crucial to obtain the final YF_3 or KY_3F_{10} crystal phase. Under acidic conditions, the slow hydrolysis of KBF_4 ensures a small concentration of F^- anions with respect to Y^{3+} cations, which yields the YF_3 phase. If the pH of the initial solution is increased, however, so are the release rate and concentration of F^- anions because the equilibrium is displaced towards the right.

Additionally, a basic media of the initial solution can lead to the precipitation of a mixture of hydroxide complexes that help to prevent Y^{3+} from the attack of other ions. Higher pH values therefore allow stabilization of the KY_3F_{10} phase rather than YF_3. Moreover, some researchers have also postulated that an acid medium can stabilize the YF_3 phase in detriment of KY_3F_{10} according to expression (7), although they obtained a mixture of the two phases [44].

$$KY_3F_{10} + H^+ \rightarrow 3YF_3 + HF + K^+ \quad (7)$$

On the other hand, with the introduction of a chelating agent (oxalic or tartaric acid in this study), the reaction takes place primarily through the Y-complex, instead of the solvated Y^{3+} ions, partially preventing the attack of other ions and thus slowing down the reaction rate to form the desired crystal phase. Nevertheless, the chelating ability of the Y-complex is weakened under hydrothermal conditions so that Y^{3+} ions can be released gradually and react with K^+ and F^- ions [45]. Therefore, the incorporation of dicarboxylic acids provides a higher concentration ratio between F^- and Y^{3+} ions, allowing the formation of the KY_3F_{10} phase at much lower pH values.

3.2. Morphological characterization

The morphology evolution of Eu^{3+}-doped YF_3/KY_3F_{10} nano/microcrystals obtained by increasing the pH in the different series of samples (with and without chelating agents) is presented in Figure 3. As shown, interesting differences appear when comparing the samples. The incorporation of surface chelators and the pH of the medium have a profound influence on the sizes and morphologies of the as-synthesized powders.

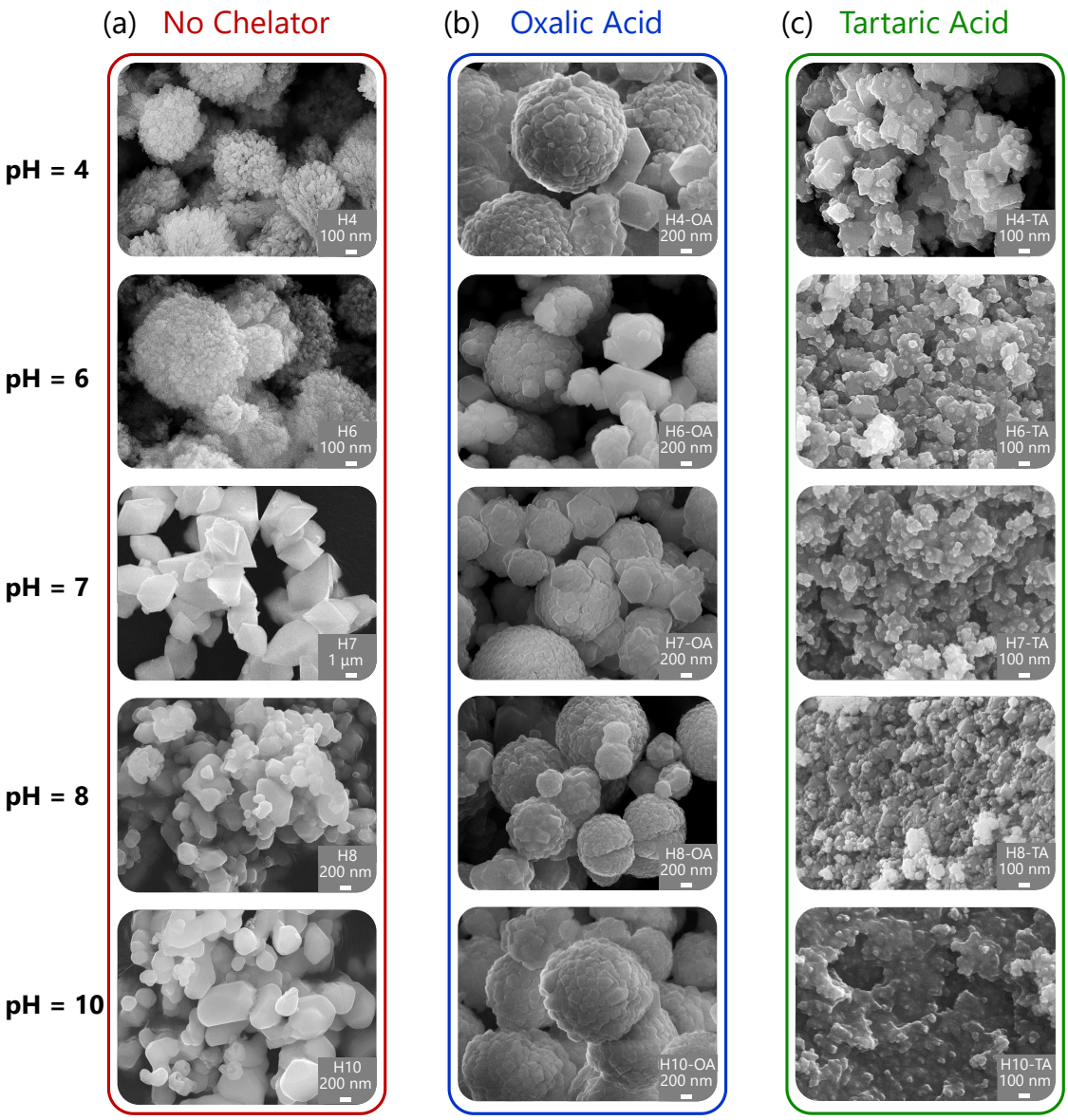

Figure 3. SEM images for the Eu^{3+}-doped samples prepared at different pH values by a hydrothermal process (a) with no chelator, (b) using oxalic acid, and (c) adding tartaric acid as a chelating agent.

3.2.1. Samples prepared without the incorporation of surface chelators

Figure 3(a) shows the SEM images of the materials prepared by the hydrothermal method without the incorporation of chelating agents. Samples H4 and H6 (YF_3 crystal structure) present very similar morphologies that can be described as self-assembled nanoparticles with an average size of 100 nm that form spheres with diameters of about 0.6 and 1.1 µm, respectively. Interestingly, when the pH of the medium is

increased to 7 (sample H7), although the crystal structure is still YF_3, the shape of the particles changes dramatically evolving toward the formation of higher crystalline ones. The as-prepared product consists of a great deal of truncated/distorted octahedra with well-defined crystallographic facets and a size that varies from 4.0 to 6.0 μm. It is also consistent with the XRD pattern of H7, which revealed a narrowing of the peaks and a change in the relative intensity of some of them in comparison to samples H4 and H6.

With regard to samples H8 and H10 (KY_3F_{10} crystal structure), their microstructure can be described as particles characterized by irregular shapes whose size increases with the pH. We found particles with a size of 0.2–0.8 μm in sample H8, while the size was slightly larger in sample H10 (0.5–1.2 μm).

3.2.2. Samples prepared with the incorporation of surface chelators

Figure 3(b) shows the SEM images of the materials prepared by the hydrothermal method with the incorporation of oxalic acid as a chelating agent. As previously mentioned in the XRD section, the introduction of OA allowed single-phase KY_3F_{10} to be obtained over the whole range of pH. In contrast to Figure 3(a), the microstructure of all the samples was very similar regardless of the acidity of the medium. Generally, the materials are composed of self-assembled nanoparticles with an average size of 200 nm that form spheres with a diameter between 1.5 and 2.0 μm. In contrast to the irregular shapes obtained without the addition of the chelating agent (samples H8 and H10), the formation of regular spheres can be attributed to the gradual and controlled release of Y^{3+} ions due to weakening of the chelating ability of the Y-complex under hydrothermal conditions, as explained previously.

On the other hand, Figure 3(c) presents the SEM images of the samples prepared by

the hydrothermal method with the incorporation of tartaric acid as a surface chelator. At first glance, the change in the surface chelator produces noticeable microstructural effects. As with the use of OA, all the samples presented the KY_3F_{10} crystal structure irrespective of the pH. The microstructure of the materials can be described as agglomerated nanospheres (50–100 nm); however, when the pH increases, so does the degree of agglomeration and sintering of the particles. The differences found between the use of OA and TA may well be explained by taking into account the synthetic experimental details described in the Supplementary Information.

Despite the fact of using chelating agents, we noted that some degree of agglomeration exists (in particular, for samples with tartaric acid). From the literature, we have found several factors that might have contributed to this phenomenon: the type of chelating agent and its chemical behavior, the molar ratio of the chelating agent to Ln^{3+}, the pH of the medium, the temperature and reaction time during the hydrothermal treatment that could favor that particles aggregate to reduce their surface energy, and the fluoride source [46–49]. All these remarks could lead to future more in-depth studies.

3.3. Photoluminescence studies

3.3.1. Excitation spectra

As per the XRD and morphological results, the optical properties were studied for samples synthesized at pH values of 4, 7, and 10 for comparison purposes. All the excitation spectra were similar. Different bands associated with the Eu^{3+} transitions were observed from the ground level $^7F_0$ to different excited levels. The relative intensities of the bands varied slightly depending on the crystal structure (YF_3 or KY_3F_{10})

(see Figure 4). Among all the transitions, the most intense was $^7F_0 \rightarrow {}^5L_6$, with a maximum at 395 nm. Therefore, the emission spectra were recorded using this value as the excitation wavelength and were normalized to the magnetic dipole $^5D_0 \rightarrow {}^7F_1$ transition.

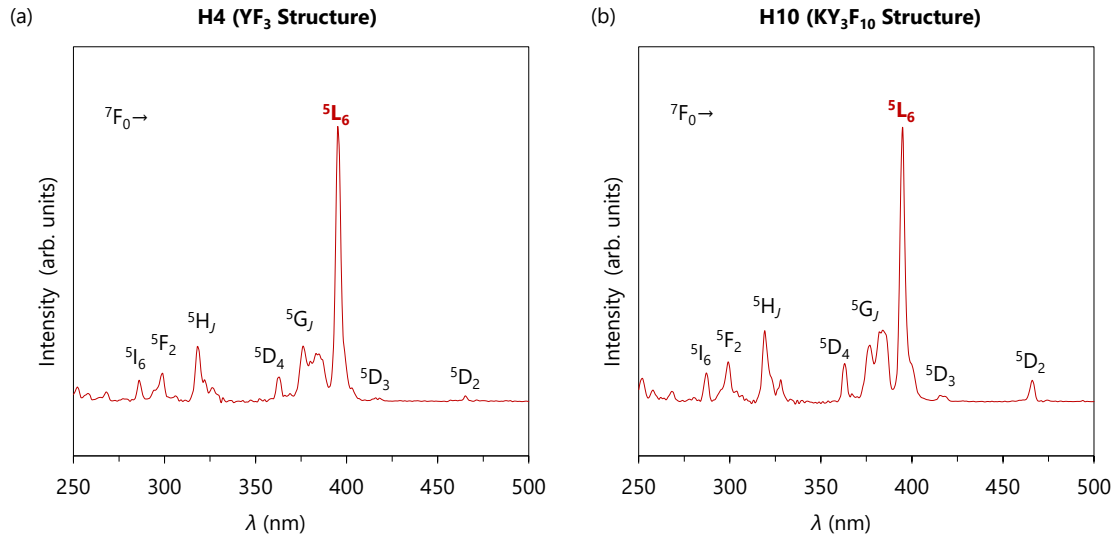

Figure 4. Room temperature excitation spectra obtained with a delay time of 0.2 ms and an emission wavelength of 593 nm for samples H4 and H10 as representatives of YF_3 and KY_3F_{10} structures, respectively.

3.3.2. Emission spectra

Figure 5 shows the room temperature emission spectra obtained with a delay time (DT) of 0.2 and 10 ms upon excitation at 395 nm for samples H4 and H10, as representatives of YF_3 and KY_3F_{10} structures, respectively. With a DT = 0.2 ms, the spectra showed a complex behavior due to the mixing of $^5D_{0-3} \rightarrow {}^7F_J$ transitions. It is worth noting that the Eu^{3+} lifetimes associated with the transitions occurring from the $^5D_{1,2,3}$ higher energy levels are expected to be lower than the lifetimes associated with transitions from the $^5D_0$ ground level. Therefore, if the detector delay time is increased to 10 ms, we can observe only the contribution of $^5D_0 \rightarrow {}^7F_J$ transitions and ensure that the assignation of bands is accurate.

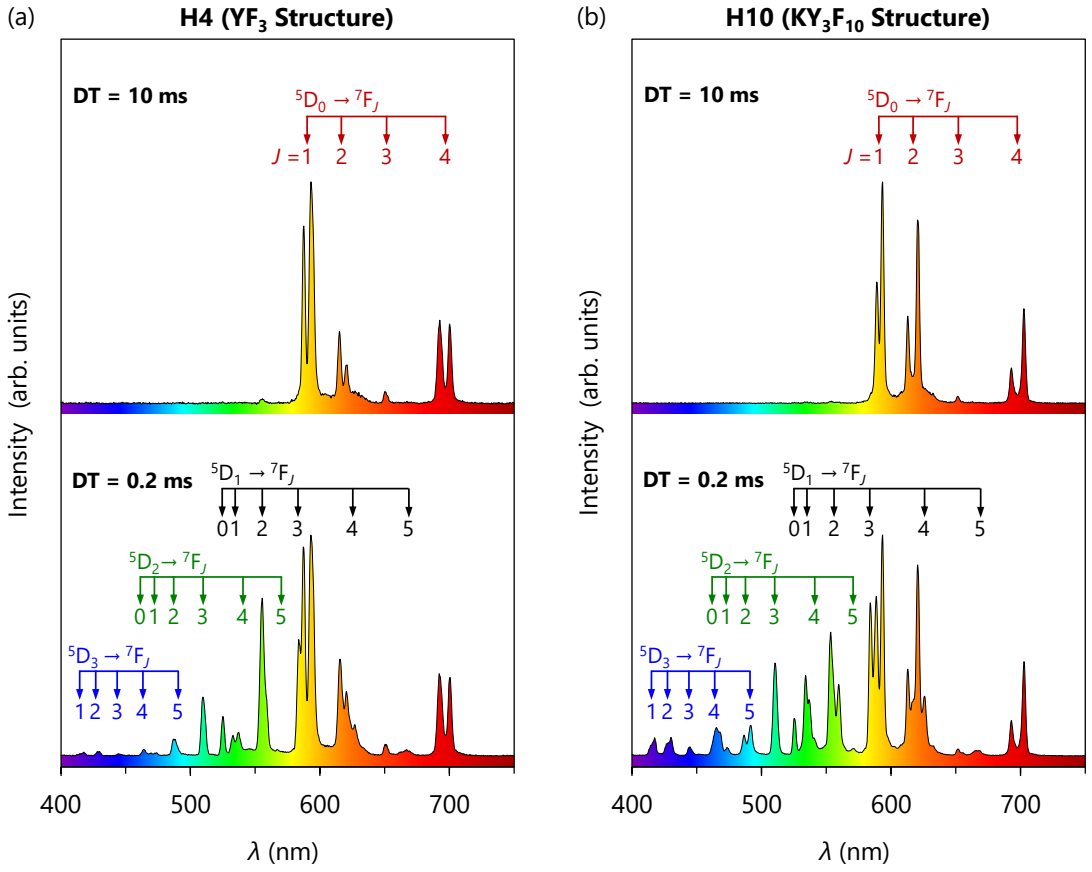

Figure 5. Room temperature emission spectra obtained with a delay time (DT) of 0.2 and 10 ms upon excitation at 395 nm for samples H4 and H10 as representatives of YF_3 and KY_3F_{10} structures, respectively. The numbers under the rows indicate the value of *J* associated with the respective transition $^5D_i \rightarrow {}^7F_J$.

The presence of bands associated with transitions occurring from the higher excited levels ($^5D_{1-3}$) is in accordance with the typical low dominant vibration frequencies available in the host lattice of fluorides [50]. As we can see from the colored plots in Figure 5, the emission lines of the Eu^{3+}-doped materials cover the whole visible spectral region: $^5D_3$ (blue), $^5D_2$ (blue-green), $^5D_1$ (green-yellow), and $^5D_0$ (orange-red). Further information about the assignation of the emission bands to their respective transitions can be found in the Supplementary Information (Section 2).

On comparing Figure 5(a) with Figure 5(b), we observe notable differences regarding the relative intensity and the splitting of the emission bands. The variation in the splitting arises from the incorporation of the Eu^{3+} ion in different symmetry sites of the

host lattice when they replace the Y^{3+} ions: C_s symmetry in the YF_3 structure, and C_{4v} in the KY_3F_{10} structure (see Figure 1 for the interpretation of the coordination polyhedra). The differences found in the relative intensity of the bands are related to the change in the crystal structure and their associated phonon energy. Therefore, it is fairly clearly demonstrated that the optical response of Eu^{3+} can be tuned by modulating the different crystal phases.

To further investigate the optical properties and analyze the variations among the different series of samples, in Figure 6(a-c) we present the emission spectra of the phosphors prepared at different pH values without the incorporation of chelating agents, using oxalic acid, or adding tartaric acid as a chelator, respectively. In general terms, all the emission spectra of samples with the same crystal structure, i.e., YF_3 or KY_3F_{10}, are similar, but some appreciations need to be considered.

In Figure 6(a), the photoluminescence modulation of the phosphors prepared with no chelators is clearly observed on comparing samples H4 and H7 (YF_3 structure) with H10 (KY_3F_{10} structure). Another important detail to note is the similitude in the emission profiles of H4 and H7, despite having a morphology and crystallinity that are extremely different, as discussed in the previous section. Referring to the oxalic acid series, Figure 6(b), no remarkable changes seem to take place when the pH is modified. However, on comparing these samples with H10, a higher degree of suppression of the $^5D_3 \rightarrow {}^7F_J$ transitions is observed. On the other hand, particular differences are found in the powders prepared using tartaric acid (see Figure 6(c)). With the increase in the pH, the intensity of the emission bands associated with transitions from the higher excited levels diminishes, a fact that can be especially apparent if we focus on the decrease in the emission line appearing at 584 nm ($^5D_1 \rightarrow {}^7F_3$), marked with red arrows in Figure 6(c).

All the above-commented differences affect the resulting emission coloration, as discussed in the following.

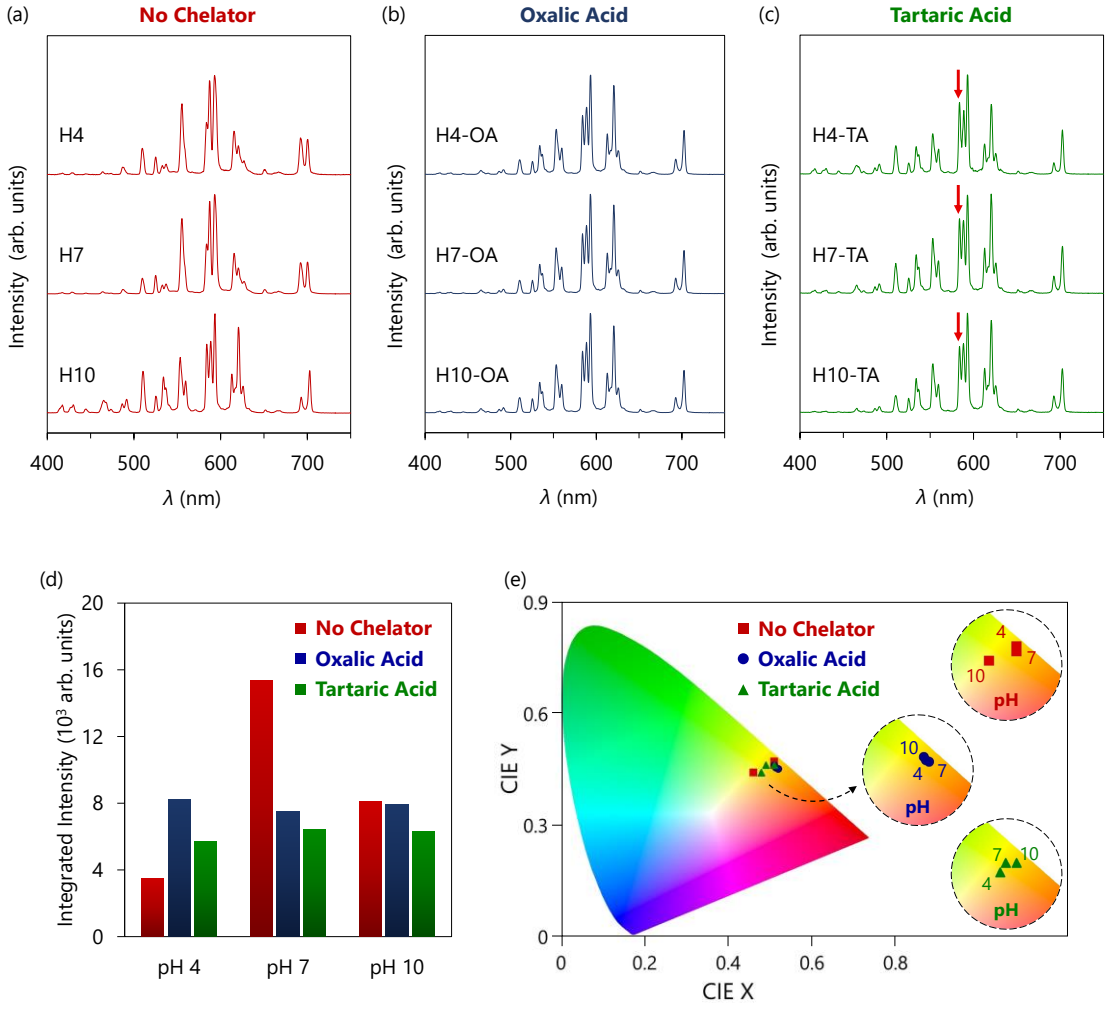

Figure 6. Room temperature emission spectra obtained with DT = 0.2 ms upon excitation at 395 nm for samples prepared at different pH values (a) with no chelators, (b) using oxalic acid, and (c) adding tartaric acid as a chelating agent. (d) Integrated luminescence intensity of the phosphors, and (e) CIE chromaticity diagram for Eu^{3+}-doped samples. The numbers in the insets indicate the pH value (4, 7, and 10).

Additionally, the bar chart in Figure 6(d) presents the values of the total integrated luminescence intensity for the different Eu^{3+}-doped phosphors. First, it is important to note that the luminescence intensity depends on several factors, such as the existence of non-radiative processes (intrinsic properties of the materials and the different crystal structures), or the scattering rate (influenced by the size and shape of particles), as

noted by G. Dantelle *et al.* [51]. On this basis, the high intensity observed in sample H7 in comparison to H4 (both with YF_3 structure) can be ascribed to a higher scattering rate, which is related to the high crystallinity and well-defined geometry of its particles [52]. In contrast, the phosphors prepared with oxalic acid have the same crystal structure (KY_3F_{10}) and particles with very similar morphologies and sizes, therefore minor changes are appreciated in the emission intensities. Similar conclusions can be drawn for the compounds prepared with tartaric acid.

Lastly, the CIE coordinates of the corresponding materials doped with Eu^{3+} were calculated from the emission spectra using the GoCIE software package [53] and are depicted in Figure 6(e). Different color emissions of the phosphors, which vary from orangish to yellow, were obtained depending on the pH and the chelating agent used. The main point is that there is a direct connection between the chromaticity and the features of the emission profiles, which can be corroborated with the insets in Figure 6(e), which corresponds to the color emission for each series of samples. For the phosphors prepared without chelators, the change in the color emission depends on the crystal phase. H4 and H7 (YF_3 structure) have a more orangish component while H10 (KY_3F_{10} structure) leads to a yellow color of the emission, closer to the white zone in the CIE diagram. As occurred with the emission spectra, no significant results are found in the series "Oxalic Acid", while a progressive evolution from yellow to orangish hues is observed for samples prepared with tartaric acid as the pH increases. This result is in perfect agreement with the onward suppression of the $^5D_{1-3} \rightarrow {}^7F_J$ transitions (blue-green region of the visible spectra). Consequently, the different tunable emissions of these compounds can be appealing for advanced applications. The technology of white light emitting diodes (w-LEDs) is nowadays attracting a lot of attention, the

combination of orange-yellow-emitting phosphors with blue InGaN chips being a common strategy to generate them [54]. Recently, fluorides have been proposed as good candidates for w-LEDs due to the high quantum efficiencies and long lifetimes of fluoride-based structures in comparison to oxide matrices [55]. Therefore, the materials synthesized in the present work could also find very interesting applications in solid-state lighting devices.

3.3.2. Judd-Ofelt and Asymmetry Ratio Calculations

According to the Judd-Ofelt theory, the transition intensities for lanthanides and actinides in solids and solutions can be explained through the calculation of different physical parameters [56]. On the one hand, the branching ratios can be used to predict the relative intensities of the emission lines originating from a given excited level and evaluate important differences among different Eu^{3+} crystal environments [57]. The experimental branching ratios for the $^5D_0 \rightarrow {}^7F_J$ transitions (β_J) can be found from the relative areas of the emission lines:

$$\beta_J(\text{experimental}) = \frac{I_{0J}}{\sum I_{0J}} \quad (8)$$

where I_{0J} is the intensity associated with the transition $^5D_0 \rightarrow {}^7F_J$ that takes place at a λ_{0J} average wavelength.

On the other hand, the intensity of the magnetic dipole $^5D_0 \rightarrow {}^7F_1$ transition is considered to be independent of the host matrix, while the electric dipole $^5D_0 \rightarrow {}^7F_2$ is known as a hypersensitive transition because it is highly influenced by the local symmetry of the Eu^{3+} ion [58]. The asymmetry ratio R is useful to analyze the local symmetry of the dopant and is defined as the ratio between the intensities of the

$^5D_0 \rightarrow {}^7F_2$ and $^5D_0 \rightarrow {}^7F_1$ transitions, which can also be related to the corresponding branching ratios:

$$R = \frac{I_{02}}{I_{01}} = \frac{\beta_2}{\beta_1} \tag{9}$$

The Judd-Ofelt parameters Ω_λ $(\lambda = 2, 4, 6)$ characterize the local structure and bonding in the vicinity of lanthanide ions. For the Eu^{3+} ion, the Judd-Ofelt parameters can be determined directly from the analysis of the emission spectra. The Ω_2 parameter correlates with the polarizable and covalent character of the lanthanide ion in the lattice (larger values of Ω_2 imply a stronger covalence) [59,60], while the Ω_4 parameter is sensitive to the viscosity and rigidity of the host lattice, which is a long-range effect. The Ω_6 parameter cannot usually be obtained from the emission spectrum due to instrumental limitations for recording the $^5D_0 \rightarrow {}^7F_6$ transition. However, the value of Ω_6 is unnecessary to predict the dynamics of the $^5D_0$ emitting manifold because its contribution to the overall transition probability is negligible [61]. The formula derived for the calculation of Ω_2 and Ω_4 Judd-Ofelt parameters is expressed as [62]:

$$\Omega_\lambda \, (\lambda = 2, 4) = A_{01} \cdot \frac{I_{0J}}{I_{01}} \cdot \frac{{\lambda_{0J}}^4}{\lambda_{01}} \cdot \frac{3h}{64e^2\pi^4 \, \chi \, \|U^\lambda\|} \tag{10}$$

where A_{01} is the magnetic dipole transition rate, which is assumed to be constant and equal to 50 s^{-1}; h is the Planck constant; e denotes the elementary charge; χ is the Lorentz local field correction term (which is equal to $\frac{n(n^2+2)^2}{9}$, where n is the refractive index at λ_{0J}); and $\|U^\lambda\|$ corresponds to the reduced matrix element of the unit tensor operator connecting levels 0–λ [63]. The value reported in the literature for $\|U^2\|$ is 0.0032 and for $\|U^4\|$ it is 0.0023 [64]. The average wavelength value obtained for the samples is 593 nm for λ_{01} ($^5D_0 \rightarrow {}^7F_1$ transition), 616 nm for λ_{02} ($^5D_0 \rightarrow {}^7F_2$ transition), and

695 nm for λ_{04} ($^5D_0 \rightarrow {}^7F_4$ transition). The refractive index of YF_3 and KY_3F_{10} is 1.49 and can be considered a constant in the spectrum range 470–700 nm [65–67]. All the calculations were performed using the data extracted from the emission spectra recorded with a DT of 10 ms to avoid the contributions from higher excited levels ($^5D_{1\text{-}3}$), which could lead to inaccurate values. The experimental branching ratios are listed in Table S1 of the Supplementary Information and the rest of the parameters are presented in Table 3.

Table 3. Asymmetry ratio values and Judd-Ofelt parameters for Eu^{3+}-doped phosphors. All the data were obtained from the emission spectra recorded with a DT of 10 ms and monitoring the excitation at 395 nm.

Sample	R	Ω_2 (10^{-20} cm^2)	Ω_4 (10^{-20} cm^2)	Ω_2/Ω_4
H4	0.33	0.60(1)	1.70(1)	0.35
H7	0.33	0.59(1)	1.56(1)	0.38
H10	1.00	1.79(2)	1.72(1)	1.04
H4-OA	1.00	1.80(2)	1.75(1)	1.03
H7-OA	1.02	1.83(2)	1.75(1)	1.05
H10-OA	1.01	1.80(2)	1.77(2)	1.02
H4-TA	1.08	1.95(3)	1.92(3)	1.02
H7-TA	1.11	2.03(3)	1.88(2)	1.08
H10-TA	1.10	1.98(3)	1.91(3)	1.04

The symmetry of the crystal site at which the dopant ions are located determines the relative intensity of the magnetic and electric dipole transitions. Lower values of the asymmetry ratio R are therefore expected for compounds in which Eu^{3+} occupies a site with an inversion center. Following the same line of reasoning, higher Ω_2 values are associated with more covalent and polarizable environments of the dopant ion, that is to say, with lower symmetric crystal sites. If we consider the replacement of Y^{3+} by Eu^{3+}

in the crystal matrices studied in this work, the site symmetry of Eu^{3+} would be C_s in the YF_3 structure and C_{4v} in the KY_3F_{10} structure. At first glance, an important change in the previous parameters can be appreciated depending on the crystal structure. Notwithstanding, the low values obtained for the asymmetry ratio (R = 0.33 for YF_3 compounds, and $R \approx 1$ for KY_3F_{10}) would not be a priori in agreement with the previous reasoning, since neither the low-symmetric point group C_s nor the C_{4v} possesses an inversion center. Nevertheless, this anomalous tendency of R has been reported to be characteristic in fluoride matrices. The higher intensity of the magnetic dipole transition $^5D_0 \rightarrow {}^7F_1$ over the electric dipole transition $^5D_0 \rightarrow {}^7F_2$ in fluorides is a result of the high iconicity of the Eu–F bonds, which allows only a little admixture of opposite parity states to the Eu^{3+} *f*-states. Thus, the $^5D_0 \rightarrow {}^7F_2$ transition becomes far less favorable as compared to, for example, the oxides [68]. On this basis, the differences found between the two crystal structures may arise from the different coordination numbers of Eu^{3+} ions and their respective changes in the iconicity of the Eu–F bonds. Indeed, the higher Ω_2 parameter for KY_3F_{10} indicates a higher degree of covalence and thus lower iconicity. Similar conclusions can be extracted from the analysis of the Judd-Ofelt parameters Ω_2 (the short-range parameter) and Ω_4 (the large-range parameter). In fact, the Ω_2/Ω_4 ratio follows the same tendency as the asymmetry ratio R.

Moreover, it is important to note that samples prepared using the same chelating agent (oxalic or tartaric acid) present similar values of R, Ω_2 and Ω_4 regardless of the pH. We can therefore assume that there are no noticeable changes in the polarizability environment of the ion, and the crystal field of Eu^{3+} must be quite similar. However, slightly higher values of these parameters are obtained for the compounds prepared

using tartaric acid. A reasonable explanation may be found taking into account the different morphology and size of the particles.

3.3.3. Lifetimes and Quantum Efficiencies Analysis

The decay curves for the different $^5D_{0-3} \rightarrow {}^7F_J$ emissions of Eu^{3+} were measured to give further information about the photoluminescence properties of the materials that were prepared. In order to analyze the observed lifetime (τ_{obs}) of the different excited levels, time-resolved luminescence measurements were performed with an excitation wavelength of 395 nm, setting a DT of 0.2 ms, and monitoring different emission wavelengths according to the respective $^5D_{0-3} \rightarrow {}^7F_J$ transitions.

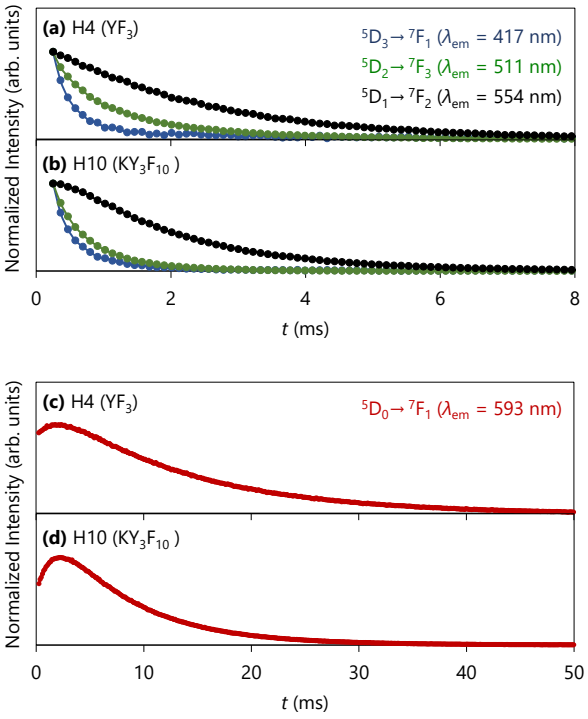

Figure 7. Normalized decay curves acquired at room temperature with a DT of 0.2 ms under the excitation of 395 nm monitoring the emission at 417 nm ($^5D_3 \rightarrow {}^7F_1$), 511 nm ($^5D_2 \rightarrow {}^7F_3$), 554 nm ($^5D_1 \rightarrow {}^7F_2$), and 593 nm ($^5D_0 \rightarrow {}^7F_1$). (a), (c) Exhibit the decay curves for sample H4; (b), (d) exhibit the decay profiles for sample H10.

Figure 7 shows examples of the decay measurements for transitions originating from

the different excited levels corresponding to samples H4 and H10 as representatives of YF_3 and KY_3F_{10} structures, respectively. An interesting feature is the presence of a rising part at the beginning of the decay profiles of the $^5D_0$ and $^5D_1$ emissions due to the Eu^{3+} population feeding from upper excited levels. The rising phenomenon is more notable for the $^5D_0$ emissions, since the emission from higher excited levels is partially quenched by cross-relaxation occurring between neighboring Eu^{3+} ions in the lattice. In this non-radiative process, the higher energy emission is quenched in favor of the lower energy level emission according to [69]. Thus, the $^5D_{0,1} \rightarrow {}^7F_J$ decay profiles were fitted using the following equation:

$$I(t) = \left[I_0 + I_1 \left(1 - \exp\left(\frac{-t}{\tau_{\text{rise}}} \right) \right) \right] \exp\left(\frac{-t}{\tau_{\text{obs}}} \right) \tag{11}$$

where I refers to the intensity as a function of time (t) and τ_{rise} is the rising time. In terms of physics, this mathematical expression can be considered a single exponential model with a modified pre-exponential factor that modulates the population of Eu^{3+} ions [70].

However, the decay curves of the $^5D_{2,3} \rightarrow {}^7F_J$ transitions were best fitted to a double exponential model without the presence of a rising part:

$$I(t) = I_1 \exp\left(\frac{-t}{\tau_{\text{obs 1}}} \right) + I_2 \exp\left(\frac{-t}{\tau_{\text{obs 2}}} \right) \tag{12}$$

The presence of these two lifetimes in the higher excited levels of the materials has been attributed to a different distribution of lanthanide ions in the crystal lattice: Eu^{3+} ions occupying the expected local symmetry and Eu^{3+} ions situated in the vicinity of a defect or impurity group in the surface of the materials [71]. When the double exponential model was used, an effective lifetime (τ_{eff}) was calculated according to:

$$\tau_{\text{eff}} = \frac{I_1(\tau_{\text{obs}\,1})^2 + I_2(\tau_{\text{obs}\,2})^2}{I_1(\tau_{\text{obs}\,1}) + I_2(\tau_{\text{obs}\,2})} \quad (13)$$

In order to evaluate the quantum efficiencies (the intrinsic quantum yields, η) of the materials, the radiative lifetimes (τ_{rad}) of Eu^{3+} ions for the $^5D_0$ level were calculated from the emission spectra recorded at a DT of 10 ms using the following expression, which is also related to the branching ratios [72–74]:

$$\tau_{\text{rad}} = \frac{I_{01}}{n^3 \cdot I_{\text{total}} \cdot (A_{01})_{\text{vac}}} = \frac{\beta_1}{n^3 \cdot (A_{01})_{\text{vac}}} \quad (14)$$

where n denotes the refractive index of the material and $(A_{01})_{\text{vac}}$ is the magnetic dipole transition rate in a vacuum (14.65 s^{-1}). The quantum efficiency of the luminescence material can be evaluated considering the calculated radiative lifetimes and the observed lifetimes for the $^5D_0$ level as follows:

$$\eta = \frac{\tau_{\text{obs}}}{\tau_{\text{rad}}} \quad (15)$$

Table 4 summarizes the lifetimes for the different excited levels ($^5D_{0–3}$) of the Eu^{3+}-doped phosphors. All the correlation coefficients of the fits (R^2) were ≥ 0.999. The calculated radiative lifetimes and quantum efficiencies for the $^5D_0$ level are also listed in Table 4. As can be appreciated, the pH and the choice of the surface chelator have a strong impact on the time-resolved luminescence of the materials, with the most remarkable effects in the lifetimes and quantum yields associated with the $^5D_0$ level.

From the experimental data, it is shown quite clearly that the lifetimes associated with the $^5D_3$, $^5D_2$, and $^5D_1$ emissions are shorter than those of the low-energy $^5D_0$ emission due to the cross-relaxation of the Eu^{3+} population at higher excited levels to

the metastable $^5D_0$ level [50]. Besides, the lifetimes of the higher excited levels ($^5D_{1–3}$) slightly decrease as the pH of the medium becomes more basic.

Regarding the $^5D_0$ level, it should be noted that the longest lifetime (12 ms) was collected for sample H4. This sample presented the YF_3 structure and was formed by self-assembled nanoparticles. In contrast, an important decrease (from 12 to 7.7 ms) is observed in sample H7, which also had the YF_3 structure and presented the highest crystallinity among all the samples studied. Another point to consider is that sample H7 also had the most intense emission, see Figure 6(d).

Table 4. $^5D_{0–3}$ lifetimes and $^5D_0$ quantum efficiencies for Eu^{3+}-doped phosphors. All the correlation coefficients of the fits (R^2) were ≥ 0.999.

Sample	$^5D_3$ (417 nm)	$^5D_2$ (511 nm)	$^5D_1$ (554 nm)	$^5D_0$ (593 nm)		
	τ_{eff} (ms)	τ_{eff} (ms)	τ_{obs} (ms)	τ_{obs} (ms)	τ_{rad} (ms)	η (%)
H4	0.95(4)	1.19(3)	2.23(1)	12.03(5)	11.53(6)	104
H7	0.76(5)	1.08(3)	1.95(1)	7.68(1)	11.83(6)	65
H10	0.64(3)	0.84(1)	1.87(1)	7.93(1)	8.45(4)	94
H4-OA	0.49(6)	0.60(1)	1.69(1)	7.18(1)	8.40(4)	85
H7-OA	0.47(4)	0.59(2)	1.71(4)	7.21(1)	8.40(4)	86
H10-OA	0.44(4)	0.57(1)	1.70(1)	7.47(1)	8.35(4)	89
H4-TA	0.58(3)	0.89(1)	1.92(1)	8.73(2)	8.02(3)	109
H7-TA	0.44(6)	0.74(6)	1.87(1)	10.11(1)	7.93(3)	127
H10-TA	0.40(3)	0.60(6)	1.85(1)	10.59(2)	7.96(3)	133

For the samples synthesized using oxalic acid, the lifetimes were about 7.2–7.5 ms, while a notable rise (up to 10.6 ms) was observed for the powders obtained using tartaric acid as a surface chelator. Powders synthesized using the same chelator (OA or

TA) had very similar integrated emission intensities, as previously noted. However, the differences in the lifetimes may be ascribed to the change in the size and morphology of the particles that can affect the electron microstructure of the samples, hence resulting in different luminescence kinetics that do not alter the emission intensity. A plausible explanation could be found considering different cross-relaxation processes of Eu^{3+} ions at higher excited levels, which could increase the $^5D_0$ population with an enhancement of the corresponding lifetime. Indeed, for samples with OA, the $^5D_3$ lifetimes do not vary so much with the increase of pH (0.49–0.44 ms) and similar values are obtained for the $^5D_0$ lifetimes.

Interestingly, apart from the H7 sample (whose behavior has been commented on above), the lifetimes of the $^5D_0$ level follow the opposite tendency with the pH in comparison to the rest of the excited levels. In this case, the lifetimes become longer as the basicity of the medium increases.

In direct connection with this, we demonstrate that the pH and the chelating agents allow us to tune the quantum efficiency of the materials to a high degree, with values in the range of 65–133%. The use of tartaric acid and the basicity of the medium enhanced the quantum efficiency of the samples. Although high values were expected due to the low phonon energy of the crystal lattices, the values higher than 100% suggest the existence of quantum cutting (QC) processes or similar energy transfers between Eu^{3+} ions that occur via cross-relaxation, as we previously noted in a recent study of Eu^{3+}-doped KY_3F_{10} materials [75]. The QC process is an interesting optical phenomenon that enables a luminescent material to convert one high-energy photon into two low-energy photons through energy transfers between ions. Thereby, the quantum efficiency of phosphors can be enhanced and reach values up to 200% [76].

The most common strategy to obtain materials with efficient QC processes involves the use of Ln^{3+} ions pairs, such as Eu^{3+}-Gd^{3+}. Efficient QC processes using only a single luminescent ion are more challenging but also possible [77–79], as evidenced in this work.

All the results lead us to confirm the extreme importance of dicarboxylic acids as surface chelators to obtain materials with different crystal phases and morphologies in a wide range of pH values. We feel that the novel use of these hydrophilic capping agents in the preparation of compounds of the KF-YF_3 system (with high relevance in photonics), instead of the commonly hydrophobic chelators, can be vital for their possible use for bioapplications. Besides, the different fluorides prepared have shown an outstanding and tunable optical response, yielding samples with very high quantum efficiencies (more than 100%) and very long lifetimes (up to 12 milliseconds). These values are totally superior in comparison to the typical oxides that are used for the fabrication of LEDs, whose efficiencies tend to be much lower and the lifetimes are usually on the microsecond scale. Therefore, the synthesized materials in the present work might have very interesting applications in solid-state lighting devices.

4. Conclusions

We prove for the first time the effective use of dicarboxylic ligands as chelating agents to modulate the surface and thus the crystal phase evolution in the KF-YF_3 system. The major conclusions that can be extracted from this study are the following:

- The crystal phase and the morphology of the Eu^{3+}-doped YF_3 and KY_3F_{10} materials prepared by a hydrothermal procedure depend critically on the pH and the chelator

used. A plausible chemical mechanism to explain the differences among the distinct series of samples has also been proposed.

- The choice of Eu^{3+} as a dopant ion and site-sensitive structural probe has allowed us to describe the optical performance of the materials properly and to establish a relationship with their chemical structure, as has been observed with the calculations of the asymmetry ratio and the Judd-Ofelt physical parameters.
- The photoluminescence of Eu^{3+} can be tuned through the different series of samples, resulting in emissions that vary from orangish to yellow hues.
- Time-resolved luminescence experiments outlined the long lifetimes of the materials (up to 12 ms). Along with that, the high quantum of these materials also showed a strong dependence on the chelator and the pH.

Based on the remarks made above, we feel that the novel use of these capping agents in such materials could arouse widespread interest, since they could also be applied to a vast gamut of compounds from the extended family of yttrium/lanthanide fluorides and find very interesting applications in bioanalytics, biomedics or photonics. Additionally, the synthesized materials in the present work, with orangish-yellow emissions, could be interesting for application in white light emitting diodes through their combination with blue chips.

Acknowledgments

The authors thank the Universitat Jaume I (Project UJI-B2019-41) and Ministerio de Economía y Competitividad (Project MAT2016-80410-P) for financial support. P. Serna also thanks the Spanish Ministerio de Ciencia, Innovación y Universidades for an FPU predoctoral contract.

References

[1] J. Wu, J. Wang, J. Lin, Y. Xiao, G. Yue, M. Huang, Z. Lan, Y. Huang, L. Fan, S. Yin, T. Sato, Dual functions of YF_3:Eu^{3+} for improving photovoltaic performance of dye-sensitized solar cells, Sci. Rep. 3 (2013) 1–5. https://doi.org/10.1038/srep02058.

[2] B.M. Tissue, Synthesis and Luminescence of Lanthanide Ions in Nanoscale Insulating Hosts, Chem. Mater. 10 (1998) 2837–2845. https://doi.org/10.1021/cm9802245.

[3] T. Grzyb, M. Węcławiak, T. Pędziński, S. Lis, Synthesis, spectroscopic and structural studies on YOF, LaOF and GdOF nanocrystals doped with Eu^{3+}, synthesized via stearic acid method, Opt. Mater. (Amst). 35 (2013) 2226–2233. https://doi.org/10.1016/j.optmat.2013.06.007.

[4] C. Sassoye, G. Patriarche, M. Mortier, High yield syntheses of reactive fluoride $K_{1-x}(Y,Ln)_xF_{1+2x}$ nanoparticles, Opt. Mater. (Amst). 31 (2009) 1177–1183. https://doi.org/10.1016/j.optmat.2008.12.013.

[5] F. Auzel, Upconversion and Anti-Stokes Processes with f and d Ions in Solids, Chem. Rev. 104 (2004) 139–173.

[6] L. Tao, W. Xu, Y. Zhu, L. Xu, H. Zhu, Y. Liu, S. Xu, P. Zhou, H. Song, Modulation of upconversion luminescence in Er^{3+}, Yb^{3+}-codoped lanthanide oxyfluoride (YOF, GdOF, LaOF) inverse opals, J. Mater. Chem. C. 2 (2014) 4186–4195. https://doi.org/10.1039/c4tc00024b.

[7] Y. Zhang, X. Li, D. Geng, M. Shang, H. Lian, Z. Cheng, J. Lin, YOF nano/micro-crystals: Morphology controlled hydrothermal synthesis and luminescence properties, CrystEngComm. 16 (2014) 2196–2204. https://doi.org/10.1039/c3ce42323a.

[8] G. Yi, H. Lu, S. Zhao, Y. Ge, W. Yang, D. Chen, L.H. Guo, Synthesis, characterization, and biological application of size-controlled nanocrystalline $NaYF_4$:Yb,Er infrared-to-visible up-conversion phosphors, Nano Lett. (2004). https://doi.org/10.1021/nl048680h.

[9] M. Deng, Y. Ma, S. Huang, G. Hu, L. Wang, Monodisperse upconversion $NaYF_4$ nanocrystals: Syntheses and bioapplications, Nano Res. 4 (2011) 685–694. https://doi.org/10.1007/s12274-011-0124-y.

[10] A. Podhorodecki, A. Noculak, M. Banski, B. Sojka, A. Zelazo, J. Misiewicz, J. Cichos, M. Karbowiak, B. Zasonska, D. Horak, B. Sikora, D. Elbaum, T. Dumych, R. Bilyy, M. Szewczyk, Lanthanides Fluorides Doped Nanocrystals for Biomedical Applications, 61 (2014) 115–125. https://doi.org/10.1149/06105.0115ecst.

[11] A. Jain, P.G.J. Fournier, V. Mendoza-Lavaniegos, P. Sengar, F.M. Guerra-Olvera, E. Iñiguez, T.G. Kretzschmar, G.A. Hirata, P. Juárez, Functionalized rare earth-doped nanoparticles for breast cancer nanodiagnostic using fluorescence and CT imaging, J. Nanobiotechnology. 16 (2018) 1–18. https://doi.org/10.1186/s12951-018-0359-9.

[12] E.N. Silva, A.P. Ayala, J.Y. Gesland, R.L. Moreira, Vibrational spectrum and lattice dynamics of KY_3F_{10} single crystals, Vib. Spectrosc. 37 (2005) 21–26. https://doi.org/10.1016/j.vibspec.2004.05.004.

[13] J. Xi, M. Ding, M. Zhang, H. Zhang, D. Chen, Z. Ji, Monodispersed YF_3:Ce^{3+}/Tb^{3+}/Eu^{3+} mesocrystals: hydrothermal synthesis and optical temperature sensing behavior, J. Mater. Sci. Mater. Electron. 28 (2017) 9489–9494. https://doi.org/10.1007/s10854-017-6692-1.

[14] J. Dabachi, M. Body, J. Dittmer, A. Rakhmatullin, F. Fayon, C. Legein, Insight into the factors influencing NMR parameters in crystalline materials from the KF-YF_3 binary system, Dalt. Trans. 48 (2019) 587–601. https://doi.org/10.1039/c8dt03241f.

[15] M. Chen, P. Loiko, J.M. Serres, S. Veronesi, M. Tonelli, M. Aguiló, F. Díaz, S.Y. Choi, J.E. Bae, F. Rotermund, S. Dai, Z. Chen, U. Griebner, V. Petrov, X. Mateos, Fluorite-type Tm^{3+}:KY_3F_{10}: A promising crystal for watt-level lasers at ~1.9 μm, J. Alloys Compd. 813 (2020) 152176. https://doi.org/10.1016/j.jallcom.2019.152176.

[16] G. Chen, H. Qiu, R. Fan, S. Hao, S. Tan, C. Yang, G. Han, Lanthanide-doped ultrasmall yttrium fluoride nanoparticles with enhanced multicolor upconversion photoluminescence, J. Mater. Chem. 22 (2012) 20190–20196. https://doi.org/10.1039/c2jm32298f.

[17] G. Murali, B.H. Lee, R.K. Mishra, J.M. Lee, S.H. Nam, Y.D. Suh, D.K. Lim, J.H. Lee, S.H. Lee, Synthesis, luminescence properties, and growth mechanisms of YF_3:Yb^{3+}/Er^{3+} nanoplates, J. Mater. Chem. C. 3 (2015) 10107–10113. https://doi.org/10.1039/c5tc02034d.

[18] Z. Gao, Z. Lai, K. Lu, S. Guo, L. Liu, F. He, P. Yang, J. Ren, J. Zhang, J. Yang, Efficient green upconversion luminescence in highly crystallized ultratransparent nano-glass ceramics containing isotropic KY_3F_{10} nanocrystals, Opt. Lett. 44 (2019) 4674. https://doi.org/10.1364/ol.44.004674.

[19] P. Villars, K. Cenzual, eds., KY_3F_{10} Crystal Structure: Datasheet from "PAULING FILE Multinaries Edition – 2012" in SpringerMaterials (https://materials.springer.com/isp/crystallographic/docs/sd_0552093)

[20] P. Villars, K. Cenzual, eds., YF_3 Crystal Structure: Datasheet from "PAULING FILE Multinaries Edition – 2012" in SpringerMaterials (https://materials.springer.com/isp/crystallographic/docs/sd_1802348)

[21] K. Momma, F. Izumi, VESTA 3 for three-dimensional visualization of crystal, volumetric and morphology data, J. Appl. Crystallogr. 44 (2011) 1272–1276. https://doi.org/10.1107/S0021889811038970.

[22] L. Zhu, Y. Liu, X. Fan, D. Yang, X. Cao, Facile synthesis and luminescence properties of uniform and monodisperse KY_3F_{10}:Ln_3(Ln=Eu, Ce, Tb) nanospheres, J. Lumin. 131 (2011) 1380–1385. https://doi.org/10.1016/j.jlumin.2011.03.024.

[23] L. Zhu, J. Meng, X. Cao, Sonochemical synthesis of monodispersed KY_3F_{10}:Eu^{3+}nanospheres with bimodal size distribution, Mater. Lett. 62 (2008) 3007–3009. https://doi.org/10.1016/j.matlet.2008.01.096.

[24] C. Cao, Hydrothermal synthesis, phase evolution, and optical properties of Eu^{3+}-doped KF-YF_3 system materials, J. Mater. Res. Soc. 27 (2012) 2988–2995. https://doi.org/10.1557/jmr.2012.331.

[25] W. Xia, J. Xiong, L. Jiang, R. Ye, Y. Mao, S. Hu, J. Yang, Lanthanide-doped KYb_3F_{10} crystals: Controllable phases, rich morphologies and Tb^{3+}/Eu^{3+} down-conversion emission, CrystEngComm. 21 (2019) 3939–3947. https://doi.org/10.1039/c9ce00420c.

[26] H. Guan, Y. Sheng, Y. Song, C. Xu, X. Zhou, K. Zheng, Z. Shi, H. Zou, YF_3:RE^{3+} (RE = Dy, Tb, Eu) Sub-microstructures: Controllable Morphology, Tunable Multicolor, and Thermal Properties, J. Phys. Chem. C. 121 (2017) 23080–23095. https://doi.org/10.1021/acs.jpcc.7b07879.

[27] L. Rao, W. Lu, H. Wang, Z. Yi, S. Zeng, Z. Li, Sub-10 nm lanthanide doped $BaLuF_5$ nanocrystals: Shape controllable synthesis , tunable multicolor emission and enhanced near-infrared upconversion luminescence, Mater. Res. Bull. 64 (2015) 27–32. https://doi.org/10.1016/j.materresbull.2014.12.033.

[28] X. Wang, J. Zhuang, Q. Peng, Y. Li, Hydrothermal Synthesis of Rare-Earth Fluoride Nanocrystals, Inorg. Chem. 45 (2006) 6661–6665. https://doi.org/10.1021/ic051683s.

[29] J. Martínez-Esaín, J. Faraudo, T. Puig, X. Obradors, J. Ros, S. Ricart, R. Yáñez, Tunable Self-Assembly of YF_3 Nanoparticles by Citrate-Mediated Ionic Bridges, J. Am. Chem. Soc. 140 (2018) 2127–2134. https://doi.org/10.1021/jacs.7b09821.

[30] C. Li, J. Yang, P. Yang, H. Lian, J. Lin, Hydrothermal Synthesis of Lanthanide Fluorides LnF_3 (Ln = La to Lu) Nano-/Microcrystals with Multiform Structures and Morphologies, Chem. Mater. 20 (2008) 4317–4326. https://doi.org/10.1021/cm800279h.

[31] H. Lin, D. Xu, A. Li, L. Yao, Z. Qiu, S. Yang, Y. Zhang, Facile synthesis and emission enhancement in $NaLuF_4$ upconversion nano/micro-crystals via Y^{3+} doping, Sci. Rep. 7 (2017) 13762. https://doi.org/10.1038/s41598-017-14228-9.

[32] Y. Guo, J. Wei, Y. Liu, T. Yang, Z. Xu, Surfactant-tuned phase crystallinity and morphologies of $NaYF_4$:Yb^{3+},Er^{3+} hexagonal microstructures and their photoluminescence properties, J. Mater. Sci. Mater. Electron. 29 (2018) 2463–2470. https://doi.org/10.1007/s10854-017-8167-9.

[33] T. Pang, M. Cai, Q. Chen, J. Xie, R. Jian, W. Lu, Regulation of phase structure, upconversion luminescence and thermal property of $NaYF_4$:Yb^{3+},Ho^{3+},Ce^{3+} through doping concentration of Ce^{3+} and Yb^{3+}, J. Alloys Compd. 789 (2019) 904–909. https://doi.org/10.1016/j.jallcom.2019.03.137.

[34] J. Yang, D. Shen, X. Li, W. Li, Y. Fang, Y. Wei, C. Yao, B. Tu, F. Zhang, D. Zhao, One-Step Hydrothermal Synthesis of Carboxyl-Functionalized Upconversion Phosphors for Bioapplications, Chem. Eur. J. 18 (2012) 13642–13650. https://doi.org/10.1002/chem.201202336.

[35] P. Qiu, R. Sun, G. Gao, B. Chen, C. Zhang, T. Yin, J. Zhang, S. Fang, D. Cui, Hydrothermal Targeted-Explosion Synthesis of Hollow/Porous Upconversion Nano- and Microcrystals with Potential for Luminescent Displays and Biological Imaging, ChemNanoMat. 1 (2015) 128–134. https://doi.org/10.1002/cnma.201400007.

[36] F. Tao, Z. Shen, Z. Wang, D. Shu, Q. Liu, Y. Sun, Oxalic Acid-Assisted Hydrothermal Synthesis and Luminescent of Hexagonal $NaYF_4$:Ln^{3+} (Ln = Sm, Eu, Yb/Er) Micro/Nanoplates, J. Nanomater. 2017 (2017) 5320989.

[37] F. Tao, Z. Zhang, J. Chen, Z. Wang, Y. Sun, Synthesis and enhancement luminescence of 3D $NaReF_4$ (Re = Eu, Sm) hierarchical microstructures assembled by nanosheets, CrystEngComm. 20 (2018) 512–519. https://doi.org/10.1039/c7ce01817g.

[38] C. Cascales, J. Fernández, R. Balda, Investigation of site-selective symmetries of Eu^{3+} ions in KPb_2Cl_5 by using optical spectroscopy, Opt. Express. 13 (2005) 2141–2152. https://doi.org/10.1364/OPEX.13.002141.

[39] R.D. Shannon, Revised Effective Ionic Radii and Systematic Studies of Interatomic Distances in Halides and Chalcogenides, Acta Crystallogr. A32 (1976) 751–767. https://doi.org/10.1107/S0567739476001551.

[40] G. Murali, S. Kaur, Y.C. Chae, M. Ramesh, J. Kim, Y.D. Suh, D.K. Lim, S.H. Lee, Monodisperse, shape-selective synthesis of YF_3:Yb^{3+}/Er^{3+} nano/microcrystals and strong upconversion luminescence of hollow microcrystals, RSC Adv. 7 (2017) 24255–24262. https://doi.org/10.1039/c7ra02188g.

[41] E. Combes, C. Sella, D. Bauer, J.L. Sabot, A study of the formation of acid and neutral yttrium oxalate powders from precipitation-stripping reaction in a Lewis-type cell, Hydrometallurgy. 46 (1997) 137–148. https://doi.org/10.1016/s0304-386x(97)00007-8.

[42] E. Combes, C. Sella, D. Bauer, J.L. Sabot, Precipitation-stripping of yttrium oxalate powders from yttrium-loaded HDEHP organic solutions using an ultrasonic stirrer, Hydrometallurgy. 46 (1997) 1–12. https://doi.org/10.1016/s0304-386x(97)00016-9.

[43] M. Zabiszak, M. Nowak, Z. Hnatejko, J. Grajewski, K. Ogawa, M.T. Kaczmarek, R. Jastrzab, Thermodynamic and spectroscopic studies of the complexes formed in tartaric acid and lanthanide (III) ions binary systems, Molecules. 25 (2020) 1121. https://doi.org/10.3390/molecules25051121.

[44] L. He, L. Xia, Y. Yang, Q. Zheng, N. Jiang, C. Xu, Y. Liu, D. Lin, Morphology-controlled synthesis, growth mechanism and fluorescence of YF3:Eu3+, Bi3+, Mater. Res. Bull. 95 (2017) 483–490. https://doi.org/10.1016/j.materresbull.2017.08.014.

[45] M. Ding, D. Chen, S. Yin, Z. Ji, J. Zhong, Y. Ni, C. Lu, Z. Xu, Simultaneous morphology manipulation and upconversion luminescence enhancement of β-$NaYF_4$:Yb^{3+}/Er^{3+} microcrystals by simply tuning the KF dosage, Sci. Rep. 5 (2015) 12745. https://doi.org/10.1038/srep12745.

[46] Z. Wang, W. Han, H. Liu, EDTA-assisted hydrothermal synthesis of cubic SrF_2 particles and their catalytic performance for the pyrolysis of 1-chloro-1,1-difluoroethane to vinylidene fluoride, CrystEngComm. 21 (2019) 1691–1700. https://doi.org/10.1039/c8ce01546e.

[47] Z. Yang, C.F. Guo, Y.Q. Chen, L. Li, T. Li, J.H. Jeong, Hydrothermal synthesis and up-conversion luminescence of Ho^{3+}/Yb^{3+} co-doped CaF_2, Chinese Phys. B. 23 (2014) 1–7. https://doi.org/10.1088/1674-1056/23/6/064212.

[48] Q. Cui, J. Xu, Synthesis and highly efficient defect-related UV-blue band luminescence of KY_3F_{10} nanocrystals, J. Mater. Sci. Mater. Electron. 27 (2016) 4372–4377. https://doi.org/10.1007/s10854-016-4306-y.

[49] S. Duhan, K. Sahoo, A. Imteyaz, S. Singh, M. Kumar, Chelating agent and substrate effect on hydrothermal growth of Yb^{3+}/Er^{3+} doped $NaYF_4$ film, Process. Appl. Ceram. 15 (2021) 69–78. https://doi.org/10.2298/pac2101069d.

[50] X. Liu, L. Yan, J. Lin, Tunable Photoluminescence and Cathodoluminescence Properties of Eu^{3+}-Doped $LaInO_3$ Nanocrystalline Phosphors, J. Electrochem. Soc. 156 (2009) 1–6. https://doi.org/10.1149/1.3002378.

[51] G. Dantelle, B. Fleury, J.P. Boilot, T. Gacoin, How to prepare the brightest luminescent coatings?, ACS Appl. Mater. Interfaces. 5 (2013) 11315–11320. https://doi.org/10.1021/am4035448.

[52] J. Adam, W. Metzger, M. Koch, P. Rogin, T. Coenen, J.S. Atchison, P. König, Light emission intensities of luminescent Y_2O_3:Eu and Gd_2O_3:Eu particles of various sizes, Nanomaterials. 7 (2017) 1–17. https://doi.org/10.3390/nano7020026.

[53] J.T. K. R., GoCIE V2, (2009). http://faculty.iitr.ac.in/~krjt8fcy/index.html.

[54] H. Wu, H. Li, L. Jiang, R. Pang, S. Zhang, D. Li, G. Liu, C. Li, J. Feng, H. Zhang, Design of a mixed-anionic-ligand system for a blue-light-excited orange-yellow emission phosphor $Ba_{1.31}Sr_{3.69}(BO_3)_3Cl:Eu^{2+}$, J. Mater. Chem. C. (2020). https://doi.org/10.1039/c9tc06360a.

[55] L.Y. Wang, E.H. Song, T.T. Deng, Y.Y. Zhou, Z.F. Liao, W.R. Zhao, B. Zhou, Q.Y. Zhang, Luminescence properties and warm white LED application of a ternary-alkaline fluoride red phosphor $K_2NaAlF_6:Mn^{4+}$, Dalt. Trans. 46 (2017) 9925–9933. https://doi.org/10.1039/c7dt02036h.

[56] B.M. Walsh, Judd-Ofelt theory: principles and practices, in: B. Di Bartolo, O. Forte (Eds.), Adv. Spectrosc. Lasers Sens., Springer, Dordrecht, 2006: pp. 403–433. https://doi.org/10.1007/1-4020-4789-4_21.

[57] P. Babu, C.K. Jayasankar, Optical spectroscopy of Eu^{3+} ions in lithium borate and lithium fluoroborate glasses, Phys. B Condens. Matter. 279 (2000) 262–281. https://doi.org/10.1016/S0921-4526(99)00876-5.

[58] K. Vuković, M. Medić, M. Sekulić, M.D. Dramićanin, Analysis of Eu^{3+} emission from Mg_2TiO_4 nanoparticles by Judd-Ofelt theory, Adv. Condens. Matter Phys. 2015 (2015) 1–7. https://doi.org/10.1155/2015/736517.

[59] D.K. Patel, B. Vishwanadh, V. Sudarsan, S.K. Kulshreshtha, Difference in the Nature of Eu^{3+} Environment in Eu^{3+}-Doped $BaTiO_3$ and $BaSnO_3$, J. Am. Ceram. Soc. 96 (2013) 3857–3861. https://doi.org/10.1111/jace.12596.

[60] C. de Mello Donegá, S.A. Junior, G.F. de Sá, Synthesis, luminescence and quantum yields of Eu(III) mixed complexes with 4,4,4-trifluoro-1-phenyl-1,3-butanedione and 1,10-phenanthroline-N-oxide, J. Alloys Compd. 250 (1997) 422–426. https://doi.org/10.1016/S0925-8388(96)02562-5.

[61] E. Cantelar, J.A. Sanz-García, A. Sanz-Martín, J.E. Muñoz Santiuste, F. Cussó, Structural , photoluminescent properties and Judd-Ofelt analysis of Eu^{3+}-activated CaF_2 nanocubes, J. Alloys Compd. 813 (2020) 152194. https://doi.org/10.1016/j.jallcom.2019.152194.

[62] P. Serna-Gallén, H. Beltrán-Mir, E. Cordoncillo, A.R. West, R. Balda, J. Fernández, Site-selective symmetries of Eu^{3+}-doped $BaTiO_3$ ceramics: a structural elucidation by optical spectroscopy, J. Mater. Chem C. 7 (2019) 13976–13985. https://doi.org/10.1039/c9tc03987b.

[63] B. Julián, J. Planelles, E. Cordoncillo, P. Escribano, P. Aschehoug, C. Sanchez, B. Viana, F. Pellé, Eu^{3+}-doped CdS nanocrystals in SiO_2 matrices: One-pot sol-gel synthesis and optical characterization, J. Mater. Chem. 16 (2006) 4612–4618. https://doi.org/10.1039/b612519k.

[64] S. Constantin, M.L. Stanciu, Calculation Of The Judd - Ofelt Parameters Of The $ZnAl_2O_4:Eu^{3+}$, Ann. West Univ. Timisoara - Phys. 56 (2012) 127–131. https://doi.org/10.1515/awutp-2015-0020.

[65] P. Porcher, P. Caro, Crystal field parameters for Eu^{3+} in KY_3F_{10}. II. Intensity parameters, J. Chem. Phys. 68 (1978) 4176–4182. https://doi.org/10.1063/1.436279.

[66] J. Zhang, Z. Hao, X. Zhang, Y. Luo, X. Ren, X.J. Wang, J. Zhang, Color tunable phosphorescence in $KY_3F_{10}:Tb^{3+}$ for x-ray or cathode-ray tubes, J. Appl. Phys. 106 (2009) 034915. https://doi.org/10.1063/1.3190511.

[67] D.F. Bezuidenhout, K.D. Clarke, R. Pretorius, The optical properties of YF_3 films, Thin Solid Films. 155 (1987) 17–30. https://doi.org/10.1016/0040-6090(87)90449-4.

[68] M.M. Lezhnina, T. Jüstel, H. Kätker, D.U. Wiechert, U.H. Kynast, Efficient luminescence from rare-earth fluoride nanoparticles with optically functional shells, Adv. Funct. Mater. 16 (2006) 935–942. https://doi.org/10.1002/adfm.200500197.

[69] T. Yamase, T. Kobayashi, M. Sugeta, H. Naruke, Europium(III) Luminescence and Intramolecular Energy Transfer Studies of Polyoxometalloeuropates, J. Phys. Chem. A. 101 (1997) 5046–5053.

[70] M.L. Debasu, D. Ananias, A.G. Macedo, J. Rocha, L.D. Carlos, Emission-decay curves, energy-transfer and effective-refractive index in $Gd_2O_3:Eu^{3+}$ nanorods, J. Phys. Chem. C. 115 (2011) 15297–15303. https://doi.org/10.1021/jp205093x.

[71] L.J.B. Erasmus, H.C. Swart, J.J. Terblans, $La_2O_2S:Eu^{3+}$ stability as temperature sensor, Appl. Surf. Sci. 487 (2019) 41–51. https://doi.org/10.1016/j.apsusc.2019.05.075.

[72] P. Ghosh, A. Patra, Influence of crystal phase and excitation wavelength on luminescence properties of Eu^{3+}-doped sodium yttrium fluoride nanocrystals, J. Phys. Chem. C. 112 (2008) 19283–19292. https://doi.org/10.1021/jp807539r.

[73] X.-N. Tian, G.-C. Jiang, X.-T. Wei, L.-Y. Wu, S. Li, K.-M. Deng, Y.H. Chen, M. Yin, Synthesis and photoluminescent properties of $NaYF_4:Eu^{3+}$ Core and

$NaYF_4$:Eu^{3+}/NaYF4 core/shell nanocrystals, J. Nanosci. Nanotechnol. 14 (2014) 4490–4494. https://doi.org/10.1166/jnn.2014.8053.

[74] M.H.V. Werts, R.T.F. Jukes, J.W. Verhoeven, The emission spectrum and the radiative lifetime of Eu^{3+} in luminescent lanthanide complexes, Phys. Chem. Chem. Phys. 4 (2002) 1542–1548. https://doi.org/10.1039/b107770h.

[75] P. Serna-Gallén, H. Beltrán-Mir, E. Cordoncillo, Tuning the optical and photoluminescence properties of high efficient Eu^{3+}-doped KY_3F_{10} phosphors by different synthetic approaches, Opt. Laser Technol. 136 (2021) 106734. https://doi.org/10.1016/j.optlastec.2020.106734.

[76] Z. Zou, L. Feng, C. Cao, J. Zhang, Y. Wang, Near-Infrared Quantum Cutting Long Persistent Luminescence, Sci. Rep. 6 (2016) 1–7. https://doi.org/10.1038/srep24884.

[77] X. Chen, J. Wu, X. Xu, Y. Zhang, N. Sawanobori, C. Zhang, Q. Pan, G.J. Salamo, Three-photon infrared quantum cutting from single species of rare-earth Er^{3+} ions in $Er_{0.3}Gd_{0.7}VO_4$ crystalline, Opt. Lett. 34 (2009) 887. https://doi.org/10.1364/ol.34.000887.

[78] X. Chen, G.J. Salamo, S. Li, J. Wang, Y. Guo, Y. Gao, L. He, H. Ma, J. Tao, P. Sun, W. Lin, Q. Liu, Two-photon, three-photon, and four-photon excellent near-infrared quantum cutting luminescence of Tm^{3+} ion activator emerged in Tm^{3+}:$YNbO_4$ powder phosphor one material simultaneously, Phys. B Condens. Matter. 479 (2015) 159–164. https://doi.org/10.1016/j.physb.2015.10.009.

[79] Y. Liu, J. Zhang, C. Zhang, J. Jiang, H. Jiang, High Efficiency Green Phosphor $Ba_9Lu_2Si_6O_{24}$:Tb^{3+}: Visible Quantum Cutting via Cross-Relaxation Energy Transfers, J. Phys. Chem. C. 120 (2016) 2362–2370. https://doi.org/10.1021/acs.jpcc.5b11790.